

# A hand-held magnetic acoustic device with integrated real-time monitoring for targeted drug delivery

Bernard Shieh, Alec Thomas, Lester Barnsley, Cameron Smith, Ashok Handa, Regent Lee, and Eleanor Stride

**Abstract**—Advances in magnetic materials have enabled the development of new therapeutic agents which can be localised by external magnetic fields. These agents offer a potential means of improving treatment targeting and reducing the toxicity-related side effects associated with systemic delivery. Achieving sufficiently high magnetic fields at clinically relevant depths in vivo, however, remains a challenge. Similarly, there is a need for techniques for real-time monitoring that do not rely on magnetic resonance imaging (MRI). Here, we present a hand-held device to meet these requirements, combining an array of permanent magnets and a thin 64-element capacitive micromachined ultrasound transducer (CMUT) interfaced to a real-time imaging system.

Drug carrier localisation was assessed by measuring the terminal velocity of magnetic microbubbles in a column of fluid above the magnetic array. It was found that the magnetic pull force was sufficient to overcome buoyancy at equivalent tissue depths of at least 35 mm and that the median terminal velocity ranged from 0.7 - 20  $\mu\text{m/s}$  over the distances measured. A Monte Carlo study was performed to estimate capture effectiveness in tumour microvessels over a range of different tissue depths and flow rates. Finally, B-mode and contrast-enhanced ultrasound imaging were demonstrated using a gel flow phantom containing a 1.6 mm diameter vessel. Real-time monitoring provided visual confirmation of retention of magnetic microbubbles along the vessel wall at a flow rate of 0.5 mL/min. These results indicate that the system can successfully retain and image magnetic microbubbles at tissue depths and flow rates relevant for clinical applications such as molecular ultrasound imaging of atherosclerosis, sonodynamic and antimetabolite cancer therapy, and clot dissolution via sonothrombolysis.

## I. INTRODUCTION

Magnetic targeting has been explored as a means of localising drug delivery and other therapies for several decades. Advances in magnetic materials, however, have reawakened interest in this approach for a range of applications [1]. The primary challenge lies in achieving magnetic field gradients strong enough for capture of magnetic particles at clinically-relevant length scales while balancing appropriate considerations for size, complexity, costs, and safety. Proposed magnet solutions include: permanent magnet assemblies (including one-sided Halbach arrays) [2]–[5], electromagnets [6], and

superconducting magnets [7], [8]. Typically, electromagnetic and superconducting systems are capable of generating very high gradient fields but do so at the expense of complexity and size owing to their large power requirements and/or the need for active cooling. Alexiou et al. [6] for example, have demonstrated a system for treating surface tumours, in which the solenoid alone occupies a cylindrical volume of 520 x 118 mm and the magnet weighs 114 kg. In contrast, permanent magnet systems lack the ability to be switched off or to generate dynamic fields with static arrangements, but they can be made much smaller, require no external power, and do not dissipate heat.

A secondary challenge is posed by the need for reliable treatment monitoring to confirm localisation of therapeutic agents at the target site and ideally quantify their concentration. MRI offers real time, three-dimensional imaging of magnetically responsive particles, but significantly increases treatment cost and complexity. It is also likely to be extremely challenging to implement simultaneously with a separate magnetic device. It should be noted that MRI systems have themselves been explored as means of drug targeting [9], [10], but cannot generate high magnetic field gradients as readily as the systems discussed above. In contrast, ultrasound imaging offers a much more convenient and lower cost method for treatment monitoring. It can be implemented using a handheld probe that can much more easily be made compatible with the magnetic targeting system. Successful imaging does however require that the magnetic drug carriers generate a sufficient acoustic impedance contrast with the surrounding tissue. This condition is likely to be met for the majority of microscale (greater than 1  $\mu\text{m}$  diameter) particles that contain a sufficient volume fraction of solid magnetic material to be effectively targeted.

There have also been extensive developments in the design of magnetic drug carriers, ranging from simple polymeric microspheres to functionalised biological cells [11]. For the purposes of this article we will focus on one type of carrier, magnetic microbubbles. These consist of a gas core surrounded by a surfactant or polymer shell into or onto which magnetic material can be incorporated. Compared with solid or liquid carriers, magnetic microbubbles offer the advantage of being highly responsive to both magnetic and acoustic stimuli. The acoustic response, resulting from the dynamic oscillation of the encapsulated gas, has well-documented utility in providing contrast in ultrasound images and in facilitating the targeted release of therapeutic agents via mechanical rupture [11].

B. Shieh, A. Thomas, C. Smith, and E. Stride are with the Institute of Biomedical Engineering, Department of Engineering Sciences, Old Road Campus Research Building, University of Oxford, Headington, Oxford OX3 7DQ, UK (e-mail: bernie.shieh@gmail.com).

L. Barnsley is with the Australian Synchrotron, ANSTO, Clayton 3168, AU.

A. Handa and R. Lee are with the Nuffield Department of Surgical Sciences, Room 6607, Level 6 John Radcliffe Hospital, University of Oxford, Oxford OX3 9DU, UK.

Furthermore, it has been shown that cavitating microbubble populations are associated with unique bioeffects, including the temporary permeabilisation of cell membranes (sonoporation) [12], cytotoxicity when combined with a sonosensitiser (sonodynamic therapy) [13], and the ability to accelerate the breakdown of clots (sonothrombolysis) [14]. The magnetic response, achieved by functionalisation with superparamagnetic nanoparticles, facilitates contrast enhancement under MRI, enables them to be guided to and accumulate within specific anatomical regions of interest, and may even serve as a source of cytotoxicity as employed in magnetic hyperthermia [15]. The synergistic combination of magnetic and acoustic responsiveness makes magnetic microbubbles an attractive platform for diagnostic and therapeutic applications. Some notable applications that have been explored in pre-clinical studies include contrast-enhanced molecular ultrasound imaging of atherosclerosis [16], site-specific gene therapy of aortic endothelial cells [17], sonodynamic and antimetabolite cancer therapy [18], and clot dissolution via sonothrombolysis [19], [20].

In previous work with magnetic microbubbles, we have demonstrated that combining a magnetic array and an ultrasound transducer into a single device facilitated better localisation of cavitation activity [3] and therapeutic effect in a murine cancer model [21] compared with separate devices applied simultaneously. This device was, however, designed for use with small animal models, enabling targeting to a depth of  $\sim 10$  mm and offered no real-time monitoring capability. Moreover, the maximum magnetic force was limited by the need to embed the piezoelectric ultrasound transducer in the face of the device. In this study, we develop a hand-held magnetic acoustic device for targeted drug delivery aimed at more clinically-relevant length scales (10 - 50 mm). The device consists of a permanent magnet array made from off-the-shelf components paired with a 64-element capacitive micromachined ultrasonic transducer (CMUT) array, the combination of which fits easily in a form factor comparable with commercial ultrasound probes. The use of a CMUT rather than a piezoelectric transducer allows the magnet to be situated as close to the target as possible. Furthermore, the CMUT enables both real-time monitoring with an image plane co-aligned with the magnetic field and the potential for delivery of therapeutic fields.

The structure of the paper is as follows. In Section II, the probe design is presented. In Section III, expressions are derived to describe the dynamics of magnetic microbubbles in magnetic fields. In Section IV, we outline the methods and procedures used to characterise and test the efficacy of magnetic targeting with our system and to demonstrate real-time monitoring capability. Finally, a discussion of the results and concluding remarks are given in Sections VI and VII, respectively.

## II. DESIGN

The device (see Fig. 1) is centred around a magnet array maximally located near the surface of the device in order to improve penetration into the body. The geometry of the

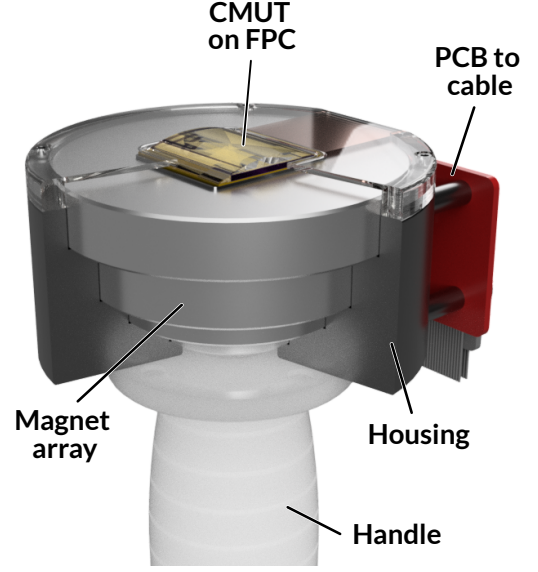


Fig. 1. 3D rendering of the magnetic acoustic device featuring a 64-element CMUT array integrated on top of a permanent magnet array.

TABLE I  
MAGNET ARRAY SPECIFICATIONS

Position (top to bottom)	Diameter (mm)	Thickness (mm)	Grade	Surface flux density (Gauss)
1	60	5	N42	1100
2	60	5	N42	1100
3	50	10	N52	2450
4	40	5	N42	1500
5	25	5	N42	2200

magnet array was optimised using a dipole model and iterative algorithm as previously described in [22]. The algorithm, set to maximise the field gradient at 50 mm from the front face of the array, was constrained to generate solutions with fixed volumes ranging from 10 to 500 cm<sup>3</sup> and with uniform magnetisation in the vertical direction, the latter of which ensured that the solutions could be realised by a self-assembling arrangement of permanent magnets. The on-axis magnetic field and normalised pull force of these solutions are shown in Fig. 2. From the set of generated solutions, the 50 cm<sup>3</sup> geometry was selected for its surface area, height, and weight which was most closely aligned with the goal of a hand-held device similar to existing commercial ultrasound imaging probes. Finally, this geometry was approximated by an arrangement of five cylindrical Neodymium (NdFeB) disks based on available off-the-shelf components (FIRST4MAGNETS, Tuxford, UK), the specifications of which are given in Table I. The total weight of the magnet array is 390 g.

To provide integrated real-time monitoring and a potential source of therapeutic pulses, a 64-element linear CMUT array (CM5-1, Philips Engineering Solutions, Amsterdam, Netherlands) was integrated above the magnet array. With a thickness (including the lens material) of just 4.2 mm, the

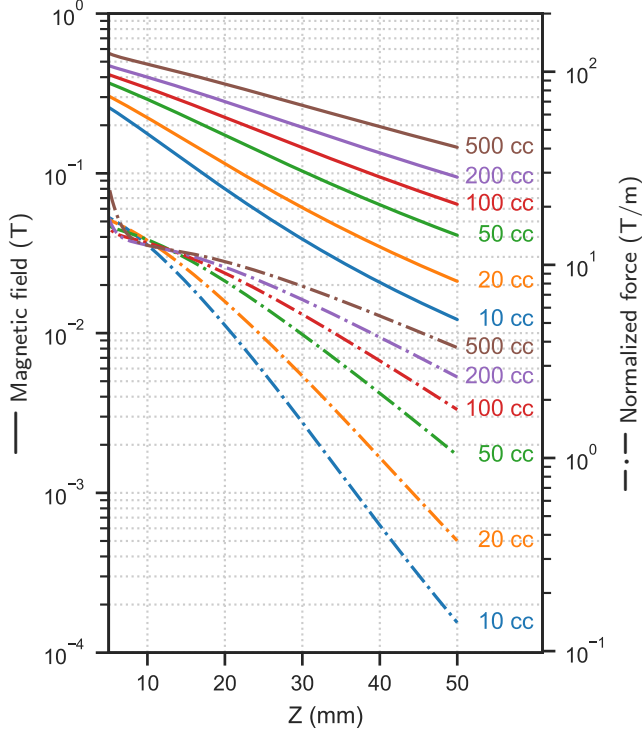


Fig. 2. Modeled on-axis magnetic field and normalised pull force as a function of depth for different magnet array volumes.

CMUT is able to provide these capabilities with minimal effect on the penetration of the magnetic field. Furthermore, the naturally wide bandwidth of the CMUT is more suited for both generation of therapeutic and diagnostic excitations. The 64-element array presents a  $21 \times 12$  mm (lateral  $\times$  elevation) aperture with an element pitch of 315  $\mu$ m. The operating band ranges from 1 - 5 MHz with a center frequency of 3 MHz. Nominal specifications for the transmit sensitivity of 0.02 MPa/V and maximum transmit pressure of 1.5 MPa were provided by the manufacturer; the imaging performance of the CMUT is described in more detail in Section V.

The CMUT is bonded to a flexible printed circuit (FPC) which routes the element connections via an intermediate adapter PCB to a 1 m long HLCD-40 high-speed cable (Samtec, Inc., New Albany, IN, USA). A second PCB interfaces the cable to a Verasonics Vantage 256 system (Verasonics, Inc., Kirkland, WA, USA) for ultrasound control and image reconstruction. The PCB also houses a HM34S programmable high voltage power supply (hivolt.de GmbH, Hamburg, Germany) which provides a current-limited adjustable bias voltage to the CMUT in the range of 0 - 200 V. The output current is limited to less than 2 mA to protect against electrical shock in accordance with EN61010-1:2010.

### III. THEORY

#### A. Dynamics of magnetic microbubbles in magnetic fields

The dynamics of a single magnetic microbubble in a fluid is governed by Newton's second law relating the microbubble's acceleration to the sum of forces resulting from buoyancy,

gravity, magnetism, and drag. The microbubble can be modelled simply as a gas-filled spherical shell of inner radius  $R_{in}$  and outer radius  $R_{out}$  composed of a mixture of lipids and nanoparticles. Let  $\rho_{gas}$ ,  $\rho_{lip}$ , and  $\rho_{np}$ , denote the densities of the gas, lipid, and nanoparticles, respectively, and let  $\alpha$  denote the fraction of the shell volume consisting of nanoparticles. Then, the effective mass of the microbubble, which includes the added mass from the surrounding fluid, is given by

$$m_{eff} = \frac{4}{3}\pi \left[ R_{in}^3 \rho_{gas} + (R_{out}^3 - R_{in}^3) ((1 - \alpha) \rho_{lip} + \alpha \rho_{np}) + \frac{1}{2} R_{out}^3 \rho_{fl} \right] \quad (1)$$

Generally, the nanoparticles experience a magnetic force in relation to its magnetic moment  $\vec{m}$  and the magnetic field  $\vec{B}$ . As the nanoparticles are small and practically isolated from one another, it can be assumed that  $\vec{m} \parallel \vec{B}$  and that the spatial variance of the moment is insignificant, i.e.  $\nabla|\vec{m}| \approx 0$ . Under this assumption, the force can be expressed as  $\vec{F}_{mag} = |\vec{m}| \nabla|\vec{B}|$ , indicating that magnetic force points from low to high field intensities. For the aggregate of superparamagnetic nanoparticles contained in the microbubble shell, the total magnetic moment can be expressed in terms of the volume magnetisation of the material which has a dependence on  $|\vec{B}|$ . The net magnet force on the microbubble can be expressed as

$$\vec{F}_{mag} = V_{mag} M_s \cdot \mathcal{L} \left( \frac{M_s V_{mag} |\vec{B}|}{k_B T} \right) \cdot \nabla(|\vec{B}|) \quad (2)$$

where  $k_B$  is Boltzmann's constant,  $T$  is the temperature in Kelvins,  $\mathcal{L}$  is the Langevin function,  $V_{mag}$  is the total volume of magnetic nanoparticles loaded onto the shell, and  $M_s$  is the saturation magnetisation of the nanoparticles, which for iron oxide is approximately  $4.7 \times 10^5$  A/m [23]. Expressions for the buoyancy and weight are straight-forward and can be found in [24].

All together, the force balance governs the motion of the microbubble and the effectiveness of external magnetic targeting. An additional simplification can be made by noting that the mass (and therefore inertia) of the microbubble is negligible in the context of physiological time scales. For example, if the magnetic force, buoyancy, and weight are grouped together as a net external force  $\vec{F}_{ext}$ , the force balance yields the following second-order ODE in terms of the position  $x(t)$  of the microbubble along the direction of the net force,

$$m_{eff} \frac{\partial^2 x}{\partial t^2} + 6\pi\mu_f R_{out} \frac{\partial x}{\partial t} = F_{ext}(t) \quad (3)$$

If the microbubble starts from rest and the net external force is constant, the solution for the velocity  $v(t)$  given by

$$v(t) = \frac{\partial x}{\partial t} = \frac{F_{ext}}{6\pi\mu_f R_{out}} (1 - e^{-t/\tau}) \quad (4)$$

The quantity  $F_{ext}/(6\pi\mu_f R_{out})$  is the terminal velocity of the microbubble and  $\tau = 6\pi\mu_f R_{out}/m_{eff}$  is a time constant characterising the rate at which the microbubble approaches its steady state velocity. For representative parameters,  $\tau \sim 3 \times$

$10^{-7}$  s. Hence, at any moment in time, it can be assumed that the microbubble travels at its drag-limited terminal velocity governed by the balance of external forces. Because the drag force on a microbubble moving at the terminal velocity is equivalent to the drag force experienced by a stationary microbubble in a flow of the same velocity, the terminal velocity also provides a direct measure of the capture effectiveness of the magnetic field. In other words, the terminal velocity is equal in magnitude to the maximum flow velocity directed away from the magnetic force in which that magnetic force is capable of holding the microbubble in place. This equivalence motivates the measurement setup described in Section IV-C to estimate the effectiveness of the magnet array in the device.

#### IV. METHODS

##### A. Characterisation of the magnetic field

The magnetic field generated by the magnet array was characterised using a 3-axis Hall sensor probe and Model 460 gaussmeter (Lake Shore Cryotronics, Westerville, OH, USA). The magnet array was secured to an optical table with its central axis oriented horizontally. From herein, unless otherwise noted, a right-handed coordinate system fixed to the front face of the magnet array is adopted with the  $+z$  direction along the central axis towards the treatment location. The  $x$  and  $y$  axes are therefore oriented in-plane with the front face, with  $+x$  defined parallel to the ground and  $+y$  directed downward. The Hall sensor probe was attached to two linear motion stages (Thorlabs Inc., Newton, NJ, USA) such that a 2D mapping of all three components of the magnetic field could be performed automatically by a raster scan. With  $y = 0$  mm, a scan was performed from  $z = 5$  mm to  $z = 45$  mm and from  $x = -20$  mm to  $x = 20$  mm, with a step size in both directions of 1 mm.

##### B. Preparation of magnetic microbubbles

A microbubble formulation utilising 1,2-dibehenoyl-sn-glycero-3-phosphocholine (DBPC) lipid and perfluorobutane (PFB) gas was chosen for its relative stability on the order of several hours [25]. DBPC and 1,2-distearoyl-sn-glycero-3-phosphoethanolamine- N- [biotinyl(polyethylene glycol)-2000] were obtained from Avanti Polar Lipids (Alabaster, AL, USA). Neutravidin protein was purchased from Thermo Fisher Scientific (Rockford, IL, USA). Decafluorobutane gas (PFB) was bought from FluoroMed (Round Rock, TX, USA). Super paramagnetic iron oxide nanoparticles (SPIONs) with a 50 nm hydrodynamic diameter were bought from Chemicell GmbH (Berlin, DE). Biotin – TEG –  $\text{NH}_2$  was purchased from Ocean Nanotech (San Diego, CA, USA). Inorganic salts, buffers, organic solvents and agar were purchased from Sigma Aldrich (St. Louis, MO, USA).

Biotinylated super paramagnetic iron oxide nanoparticles were made in house by covalent linkage of the carboxymethyl functional group on the nanoparticle with Biotin-TEG- $\text{NH}_2$ . All lipid suspensions were prepared at a 9:1 molar ratio of DBPC:DSPE-PEG2000-Biotin at final lipid concentration of 5 mg/mL in a 15% propylene glycol phosphate buffered solution. Lipid solutions were heated to  $85^\circ\text{C}$  for one hour

under constant stirring. The lipid solution was then probe sonicated at low power for 2 minutes (QSonica Q125, 20 kHz, 3 mm probe tip, amplitude: 20%, 30 second intervals) with the tip submerged. The tip was then moved to the air water interface and PFB gas was flown in the head space for 10 seconds before sonicating the solution at 90% power for 15 seconds. The glass vial was then immediately removed and placed on ice for 10 minutes.

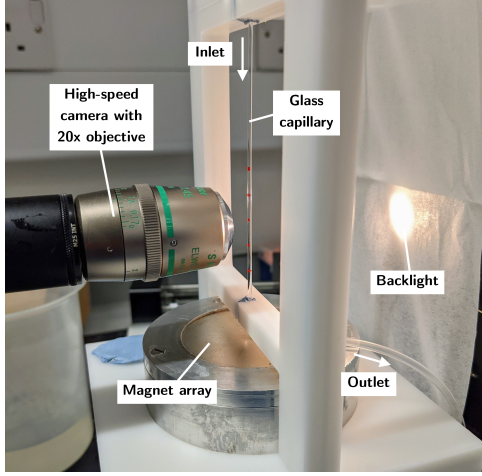
To wash off unbound lipid, bubbles were centrifuged at 350 RCF for 5 minutes in a 5 mL syringe. After each cycle, the subnatant, which appeared as a white foam, was discarded by depressing the plunger and the supernatant was resuspended to 5 mL at  $4^\circ\text{C}$ . The process was repeated three times for each wash cycle. Biotinylated microbubbles were then mixed with 0.5 mg/mL neutravidin solution for 10 minutes at  $4^\circ\text{C}$ . To remove unbound avidin, three wash cycles were completed. Then biotinylated nanoparticles were diluted 10-fold to a final volume of 2 mL and mixed with the microbubble supernatant for 10 minutes at  $4^\circ\text{C}$ . To wash off unbound nanoparticles, a wash cycle was completed. Removal of microbubbles larger than 5  $\mu\text{m}$  in diameter was then completed by centrifugation at 180 RCF for 1 minute. In this case, the subnatant was retained and the supernatant was discarded, this process was repeated twice. The size distribution and concentration were measured before and after the removal of the greater than 5  $\mu\text{m}$  microbubble population (Multisizer 4e, Beckman Coulter, Indianapolis, IN, USA). In all the following experiments, microbubbles were prepared and stored at  $4^\circ\text{C}$  in concentrated form in order to preserve their integrity against dissolution and Ostwald ripening. The microbubbles were always used within 4 hours of preparation.

##### C. Terminal velocity measurement of magnetic microbubbles in the magnetic field

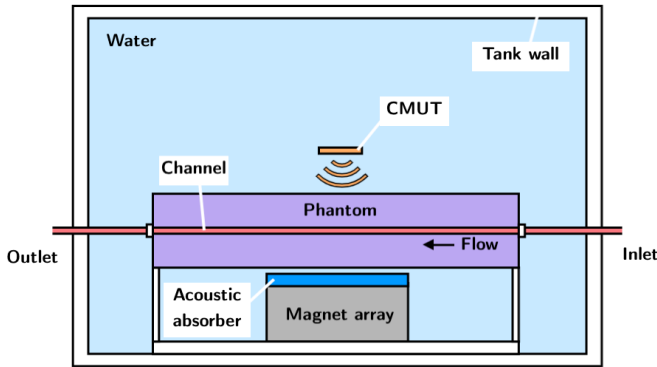
A setup was devised (see Fig. 3a) to measure the terminal velocity of magnetic microbubbles falling or rising while under the influence of the magnet array positioned below. By measuring the distribution of terminal velocities for a given microbubble population, an estimate could be determined for the maximum flow velocity in which the magnet array has sufficient influence to attract microbubbles. Here, capture is defined in the worst-case scenario where the flow and buoyancy force are directly opposed to the magnetic force. Furthermore, in comparison to measuring capture in phantoms mimicking physiological geometries, this experiment eliminates geometry-dependent variables and defines capture in relation only to the fundamental forces on the microbubble. The maximum flow velocity determined in this way could be useful in gauging capture effectiveness from simulations of flow fields in more complex geometries.

The setup consisted of a glass capillary (0.6 mm ID, 1.5 mm OD) attached at both ends to a plastic frame. The frame was affixed to the magnetic array so that its central axis and the capillary were collinear. Lines were drawn on the capillary demarcating distances to the front face of the magnet array at 17, 25, 35, and 45 mm. Flexible tubing was attached to the top of the capillary for inflow and to the bottom of the capillary as





(a) Terminal velocity measurement setup



(b) Real-time monitoring in flow phantom setup

Fig. 3. (a) Experimental setup used to measure the terminal velocity of magnetic microbubbles under the influence of the magnet array. (b) Top-down diagram of the water tank setup used to demonstrate real-time monitoring and microbubble retention in a tissue-mimicking flow phantom.

a drain path. Following a flush with phosphate-buffered saline (PBS), a 1.5 mL solution of magnetic microbubbles with a concentration of  $1 \times 10^7$  MB/mL was introduced from the top using a syringe. A Master-Flex continuous cycle syringe pump (Cole Palmer, UK) was used to flow in the solution at a rate of [rate] mL/s after which an inline ball valve was closed in order to arrest fluid motion. A Memrecam HX-5 high-speed camera (Nac, Tokyo, JP) with a 20x objective (Nikon, Tokyo, JP) was positioned in front of the capillary with a backlight illuminating the rear in order to capture video of the microbubbles. For each injection, three videos were recorded in order to track the evolution of the microbubble population over time. Each video was recorded at 50 fps with an approximate duration of 15 s. The videos were started at 30, 180, and 420 s after closure of the ball valve. Because the imaging field of view was limited to approximately 100  $\mu\text{m}$ , the height of the capillary and magnet array assembly was adjusted using a manual positioning stage to each of the four demarcated distances. The experiment was repeated both at each distance and in the absence of the magnet array, the latter which served as a control.

To obtain estimates for the terminal velocity of the microbubbles, the trajectories of the populations captured in each

video were extracted through a series of processing steps. First, a stationary background frame was extracted from a video of the capillary filled with PBS and no microbubbles. Blob detection (OpenCV [26]) was performed on this background frame to identify the positions of bubble-like objects, most likely dust and scratches on the lens and sensor, which would otherwise be registered as false positives. This background frame was also subtracted from all the frames by a factor of 80% to help isolate microbubbles from stationary background features. Contrast limited adaptive histogram equalisation (CLAHE, OpenCV) was applied to each frame with a tile width and height of 40 px to equalise spatial variations in lighting. Next, microbubbles were identified in the first frame using blob detection and their positions logged. Any position overlapping the location of a background object (collision radius of 30 px) was ignored. This ROI identification process was repeated every five frames to register new microbubbles entering the FOV. Finally, valid positions were handed off to a tracking algorithm (Kernelised Correlation Filter, OpenCV) for motion tracking in subsequent frames. The average velocity of each tracked microbubble was calculated from the logged positions, where the width of each pixel was determined to be 693 nm by calibration with a hemocytometer. Tracking was limited to a 1450 px wide and 725 px high area centered in the FOV to reduce fluid boundary effects. Only objects successfully tracked for at least 1 s (50 frames) were considered in the analysis.

#### D. Monte Carlo simulation of microbubble retention in a microvessel

A common aim of magnetic delivery is the transport and retention of therapeutic agents in the tumour microenvironment for the purposes of targeted treatment [18], [21]. Tumour vascular networks are characterised by a highly irregular morphology in which blood flow velocities may be an order of magnitude lower than in normal vessels [27]. We model retention in an idealised tumour microvessel represented simply by a cylindrical lumen with flow directed parallel to the front face of the magnet array [24]. Here, because the predominant component of the pull force is orthogonal to the direction of flow, capture is dictated by the ability of the magnet to attract microbubbles to resting positions along the lumen wall within the limited time spent in the magnetic field.

For this study, we modeled a 2 cm long microvessel section with a central axis located 20, 30, and 40 mm above the front face of the magnet array. The microvessel diameter was varied from 1 – 50  $\mu\text{m}$  and the flow velocity was varied from 0.1 – 4 mm/s in order to cover a wide range of geometries as reported by animal studies [28]–[31]. The flow was assumed to be laminar, with a parabolic profile described by

$$v_{fl}(r) = 2\bar{v}_{fl} \left[ 1 - \left( \frac{r}{R} \right)^2 \right] \quad (5)$$

where  $r$  is the distance to the central axis,  $R$  is the capillary radius, and  $\bar{v}_{fl}$  is the mean flow speed.

With flow directed to the right, simulated microbubbles were positioned at the inlet boundary with position randomly sampled with uniform probability over the circular cross-sectional

TABLE II  
MONTE CARLO SIMULATION PARAMETERS

Symbol	Description	Value	Units
$\rho_{gas}$	Gas density	11.2	$kg \cdot m^{-3}$
$\rho_{lip}$	Lipid density	1097	$kg \cdot m^{-3}$
$\rho_{np}$	SPION density	5240	$kg \cdot m^{-3}$
$\rho_{fl}$	Fluid density	1060	$kg \cdot m^{-3}$
$R_{out} - R_{in}$	Shell radius	55	$nm$
$M_s$	SPION magnetisation	$4.7 \times 10^5$	$A \cdot m^{-3}$
$\alpha$	SPION loading fraction	0.1	-
$\mu_{fl}$	Fluid dynamic viscosity	$2.78 \times 10^{-3}$	$Pa \cdot s$
$T$	Temperature	310	$K$

area and with initial velocity given by (5). The trajectories of each microbubble were determined independently by numerical integration of (3) with  $m_{eff} \approx 0$  using an implicit Adam's method [32]. External forces were evaluated with buoyancy and gravity directed upward and downward, respectively, and with the magnetic force calculated using (2) where the spatial variation of the field was determined by interpolation of the experimentally-characterised field. Microbubbles were considered captured if their trajectories terminated at the bottom half of the capillary within the allotted 2 cm length.

The material properties of the microbubbles used in the simulation are given in Table II. Note that the nanoparticle loading fraction was set to the theoretical maximum of 0.1 based on the number of available binding sites on the shell. To account for variations in microbubble size, microbubble diameters were selected randomly from a probability density function matching the distribution measured in the experiments. The measured diameter distribution had the following four moments: mean of 1.7  $\mu m$ , standard deviation of 0.69  $\mu m$ , skew of 1.0, and kurtosis of 0.89. For each combination of capillary distance, capillary diameter, and mean flow velocity, 3000 microbubble trajectories were simulated and the percentage captured was recorded.

#### E. Real-time monitoring of microbubble capture in a flow phantom

The 64-element CMUT with full element connectivity is an enabling platform for real-time monitoring, making it possible to realise a variety of imaging techniques such as B-mode, colour flow doppler, contrast enhanced ultrasound (CEUS), and passive acoustic mapping (PAM). We demonstrate a subset of these capabilities by implementing real-time multi-focal B-mode imaging and pulse inversion contrast enhanced ultrasound (PICEUS). B-mode images were reconstructed at 4 MHz for a 60° sector scan with 6 cm depth using 180 ray lines. Each image frame was synthesised using three focal zones in transmit and fully synthetic per pixel focusing in receive. Imaging performance was assessed using a Model 539 multipurpose phantom (ATS Laboratories, Norfolk, VA USA). Implementation of CEUS with CMUTs is an ongoing challenge due to their inherent drive non-

linearity which generates undesirable harmonic content that is difficult to distinguish from that generated by contrast agents and tissue [33]. However, it has been shown that CMUT non-linearity obeys a power series relationship, a property which can be exploited by pulse inversion to remove spectral content from the fundamental and odd harmonic bands [34]. For example, consider a simple model of CMUT actuation where the predominant source of non-linearity comes from the dependence of the force on the square of the voltage. The voltage  $v(t)$  can be expressed as

$$v(t) = v_{dc} + v_{ac}w(t)\cos(\omega t + \phi) \quad (6)$$

where  $v_{dc}$  is the bias voltage, and the excitation is expressed as an enveloped cosine with amplitude  $v_{ac}$ , envelope  $w(t)$ , carrier frequency  $\omega$ , and phase  $\phi$ . Then, the force/voltage relationship is given by

$$\begin{aligned} f(t) \propto v^2(t) &= v_{dc}^2 + \frac{v_{ac}^2}{2}w^2(t) \\ &+ 2v_{dc}v_{ac}w(t)\cos(\omega t + \phi) \\ &+ \frac{v_{ac}^2}{2}w^2(t)\cos(2\omega t + 2\phi) \end{aligned} \quad (7)$$

which predicts the generation of subharmonic, fundamental, and second harmonic bands. With pulse inversion, in which echoes generated by the standard excitation are summed with that generated from an excitation with inverted polarity, the fundamental band is eliminated while the other contributions are doubled. Echoes generated from microbubbles do not obey the power series relationship, opening up the fundamental band for detection of these agents. However, (7) also predicts that the bandwidth of the subharmonic and second harmonic contributions will be broadened as a result of the squaring of the envelope, indicating the potential for overlap with the fundamental band which may degrade dynamic range. Even worse, digital transmit pulse synthesis commonly found in commercial ultrasound systems may broaden these contributions due to spectral leakage [35], [36].

We utilised a simple strategy to overcome these challenges. First, the excitation was centred at 4 MHz to increase the separation of the subharmonic and second harmonic bands. Second, spectral leakage of the pulse was minimised by using a digital pulse sequence designed using the Arbitrary Waveform Toolbox (AWT) (Verasonics, Inc., Kirkland, WA USA). The AWT-optimised digital pulse results in more gaussian-like spectral output from the transducer with reduced energy in the second harmonic band. Finally, the received RF data were bandpass filtered around the fundamental before image reconstruction.

PICEUS was demonstrated in a flow phantom featuring a single 1.6 mm diameter channel. The phantom was prepared according to a recipe that mimics the ultrasonic properties of tissue [37]. Briefly, the preparation (% weight) consisted of: 82.97% water, 11.21% glycerol (Sigma, UK), 3.0% agar (Top Vision, ThermoFisher, UK), 0.74% 400 grain SiC powder, 1% 3  $\mu m$   $Al_2O_3$  powder, and 1.08% 0.3  $\mu m$   $Al_2O_3$  powder. The phantom was sandwiched between two Mylar sheets for waterproofing and probe access with an effective window of 20 cm by 20 cm and thickness of 1 cm. A diagram of the

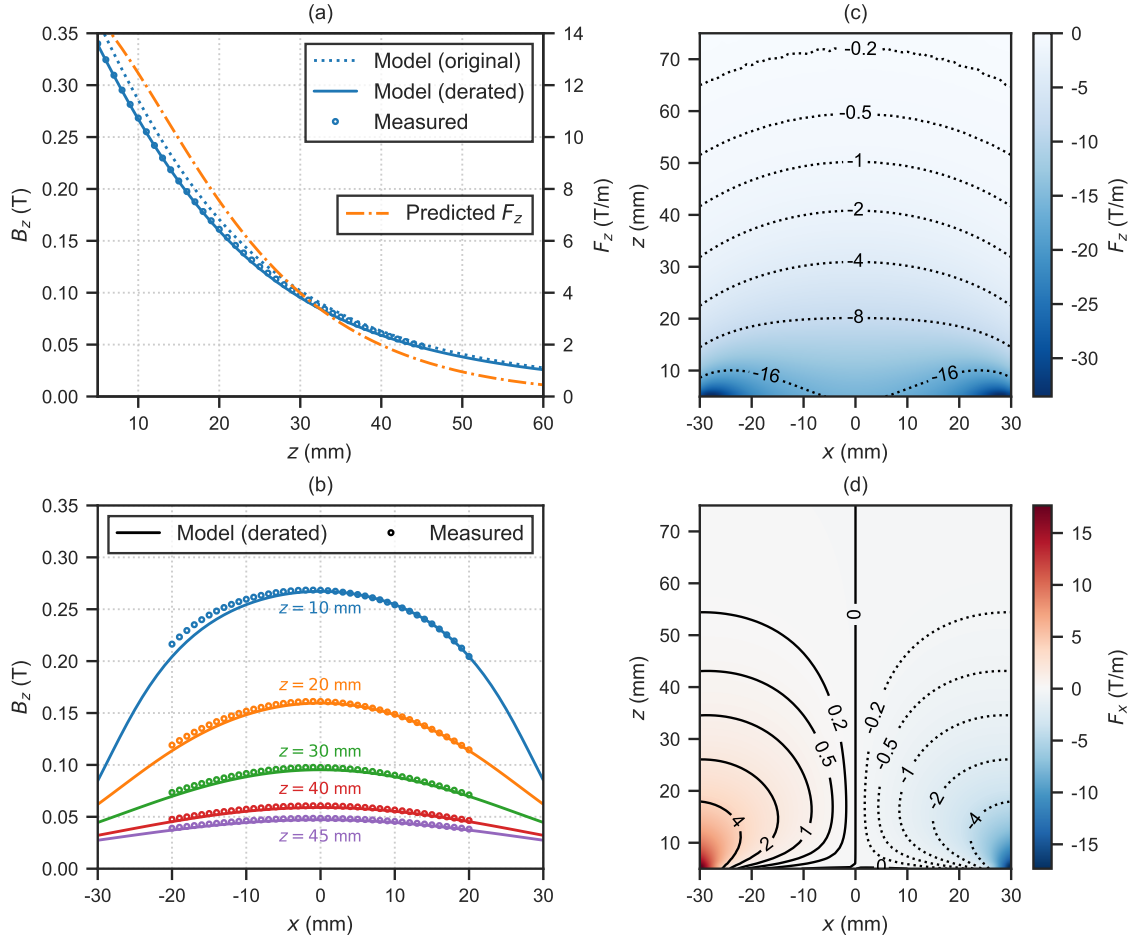


Fig. 4. (a) On-axis magnetic field characterised by hall probe measurements and then compared with the original modelled field and the field derated by a factor of 0.935. The on-axis normalised pull force predicted by the derated field is also shown. (b) Measured field compared with the derated modelled field lateral variation at different distances from the magnet array. (c) A spatial map of the normalised pull force derived from magnetic field measurements. (d) A spatial map of the normalised lateral force derived from magnetic field measurements.

experimental setup used with the phantom is provided in Fig. 3b. The phantom was placed in a plastic frame rigidly mounted to the magnet array such that the channel sat 3 cm above the face of the magnet array with its flow direction parallel to the face. Acoustic absorbing material was placed between the phantom and the magnet array to reduce reflected echoes in the image. The entire assembly was then placed inside a water tank with the central axis of the magnet array and the flow direction both parallel to the ground, i.e. such that buoyancy and gravity forces were orthogonal to the magnetic pull force. Due to limitations with the mounting apparatus on the tank, the CMUT and magnet array were not oriented in their intended configuration with the CMUT directly on top of the magnet surface. Rather, the CMUT was lowered in the tank on the opposing side of the phantom and oriented to image the phantom at an approximate distance of 3 cm from the channel.

Four cases with the phantom were performed: B-mode with no magnet present (control), PICEUS with no magnet present (control), B-mode with the magnet present, and PICEUS with the magnet present. In each case, a 511  $\mu\text{L}$  bolus injection of

magnetic microbubbles suspended in PBS was introduced at the inlet of the channel, corresponding to a concentration of  $1 \times 10^7$  MB/mL. A syringe pump was used to flow the bolus, followed by PBS, into the channel at a rate of 0.5 mL/min for a total volume of 3 mL. Real-time images were recorded at the start of the flow and for approximately 6 min after. Prior to and between cases, the channel was flushed with 30 mL of deionised water and 4 mL of PBS in order to clean and remove any residual microbubbles left in the channel.

## V. RESULTS

### A. Characterisation of the magnetic field

A comparison of the measured on-axis magnetic field and the original modelled field is shown in Fig. 4a. In order for the measurements to align with our model, it was necessary to introduce a constant deration factor of 0.935 to the modelled results, chosen to minimise the mean-squared error between the modelled and measured fields. The lower than expected field can be attributed to the use of off-the-shelf magnetic discs, some of which were not of the highest grade, and the fact that the chosen disc dimensions were only an approximation of

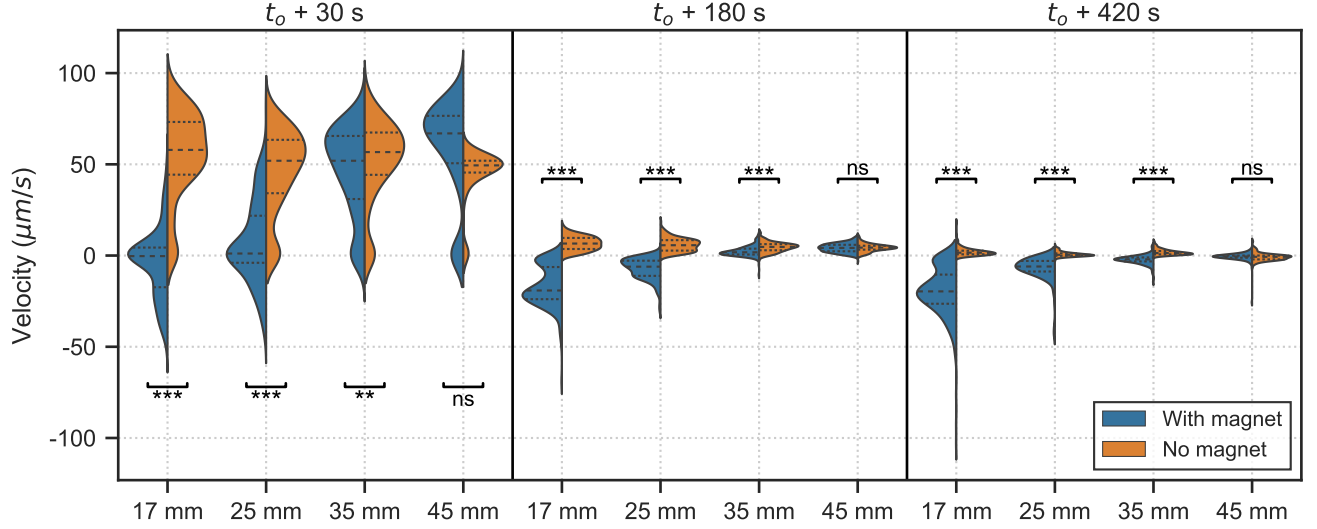


Fig. 5. Terminal velocity distributions for magnetic microbubble populations in a vertical fluid column with and without the magnet array. The velocities were recorded at elapsed times of 30, 180, and 420 seconds after the introduction of microbubbles into the column and at different distances above the magnet array. The mean of each distribution is indicated by a dashed line and the quartiles by dotted lines.

the optimised geometry. With the deration factor accounted for, the spatial variation of the field along both  $x$  and  $z$  are in good agreement with the model. Measurements indicate an on-axis field of 0.1 T at 3 cm with a normalised pull force of 4 T/m. Lateral variation of the field, depicted in Fig. 4b, indicate good uniformity, with a FWHM exceeding the measurement range of  $-20$  to  $20$  mm. Spatial maps of the normalised force in both  $x$  and  $z$  were generated from the model and are shown in Fig. 4c and Fig. 4d. The maps depict a large area of effect spanning the diameter of the magnet array.

### B. Terminal velocity measurement of magnetic microbubbles in the magnetic field

The terminal velocity distributions extracted from the videos at different distances from the magnet array and at different elapsed times after introduction of microbubbles are shown in Fig. 5. At each distance and time, the distributions are drawn for the case with the magnet array on the left and without the magnet array (control) on the right. The sample size of the distributions ranged from 151 to 351 samples, depending on the number of microbubbles which could be successfully tracked in each video. Focusing just on the controls, it is generally observed that the distributions change significantly over time, with the population skewed strongly toward positive velocities at 30 s after  $t_o$ . Furthermore, the distributions at this time are bimodal, with a population centred at a large positive velocity near  $50 \mu\text{m/s}$  and a smaller population near  $0 \mu\text{m/s}$ . There are two effects which we hypothesise may be responsible for these observations. First, bulk fluid motion in the column is likely to occur shortly after  $t_o$  as a result of mechanical fluctuations in the system, e.g. pressure surge due to the closing of the ball valve, and residual vibrations in the tubing attached to the column. Second, reduced viscous drag due to the wake of nearby microbubbles could artificially

increase the terminal velocity of the population. This effect would be more pronounced at earlier times, as the size of the population is the highest at  $t_o$  and is expected to decrease as the population of strongly buoyant microbubbles in the column is exhausted. The finiteness of the population can be explained by bends in the tubing at the bottom of the column which could prevent microbubbles from entering the column via the bottom. A by-product of this effect is that some buoyant microbubbles may experience negative velocities as a result of being pushed downward from opposing flow. Due to these postulated effects, the terminal velocity distributions at 30 s and 420 s after  $t_o$  may not accurately capture the terminal velocities of the microbubble population. Therefore, in evaluating the effect of the magnet array, we restrict our attention to the measurements taken 420 s after  $t_o$ .

One-sided Welch's t-tests were performed on the sample means to determine the effectiveness of the magnet array in reducing the terminal velocity in comparison with the control. This test was chosen due to the different sample sizes and the differing variance between the populations being compared, the latter which is evident in Fig. 5. A statistically significant effect was observed at each distance up to 35 mm, while no significant effect was observed at 45 mm. The 98% confidence intervals of the mean for 17, 25, and 35 mm distances were  $(-21, -18)$ ,  $(-8.1, -6.2)$ , and  $(-2.7, -1.8) \mu\text{m/s}$ , respectively, indicating that at these distances, on average, the effect was sufficient to overcome buoyancy.

In Fig. 6, we compare the experimental velocity distributions at 420 s after  $t_o$  to modelled distributions based on (1), (2), and (4). The underlying variance in microbubble radius was taken into account using the measured population size distribution. Because the variance in the SPION loading fraction could not be measured directly, the theoretically maximum of 0.1 was assumed. The median, interquartile range (IQR), and



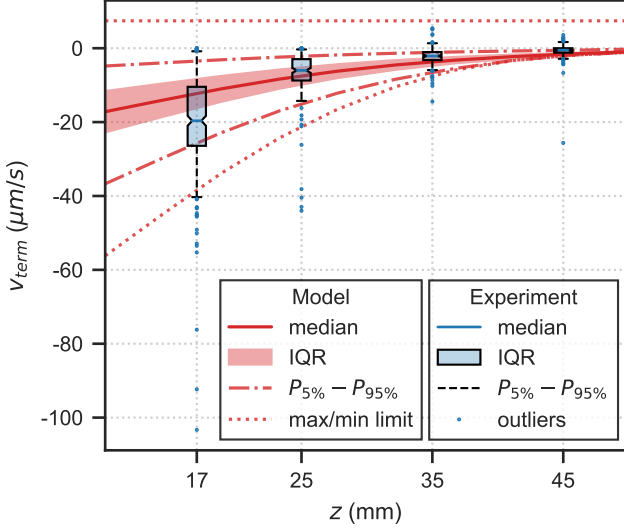


Fig. 6. Comparison between modelled and experimental measurements of the terminal velocity distribution at different distances. The experimental distributions shown correspond to terminal velocities measured at 420 seconds after the introduction of microbubbles.

5% and 95% percentile velocities are shown for the modelled distributions, along with the velocities corresponding to the theoretical minimum (maximum loading fraction and optimal radius with respect to the force balance) and maximum (unloaded with maximum radius). The experimental distributions are represented with box-and-whiskers with outliers defined as individuals beyond the 5% and 95% percentile limits.

At all distances except 17 mm, the measured median velocity was slightly smaller in magnitude than that predicted by the model, likely indicating a median loading fraction of SPIONs on the microbubbles lower than the ideal value. At a distance of 17 mm, however, the median velocity is larger in magnitude, with the distribution skewed downward. It is possible that the microbubble population measured is no longer representative of the initial population due to the presence of the magnetic field and the elapsed time having a selective effect on migration of microbubbles in the capillary. Finally, aggregation may be responsible for the observed outliers as the formation of microbubble chains was detected visually in the videos. The chain structure may be advantageous as a means for increasing the loading of magnetic material while only marginally increasing drag. The observed results suggest that the terminal velocity of these microbubble trains could be up to 2.5 times higher than the theoretical limit for individual microbubbles.

#### C. Monte Carlo simulation of microbubble retention in a microvessel

Stochastic modelling of microbubble trajectories provide an estimate of the ability of our magnetic delivery system to capture microbubbles in the tumour microenvironment. The percentage of microbubbles captured according to our model for varying microvessel diameter, flow velocity, and distance from the magnet are shown in Fig. 7. It is observed that the

Percent of simulated microbubbles captured

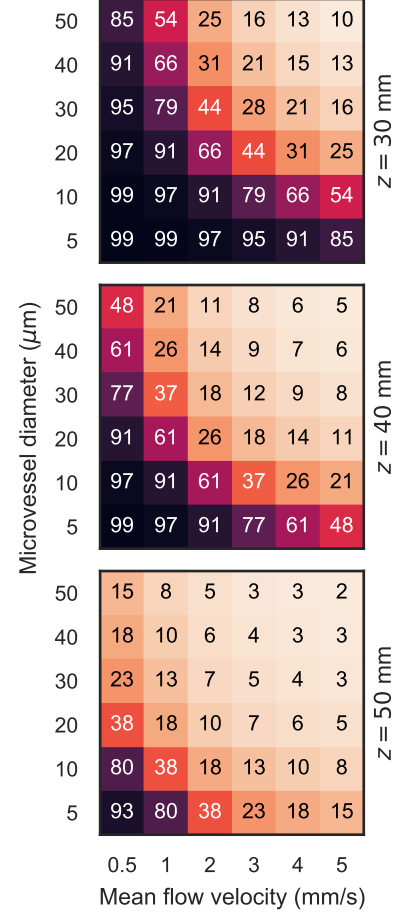


Fig. 7. Simulated percentage of microbubbles captured in a capillary for different microvessel diameters, flow velocities, and distances from the magnet array.

capture percentage has the same functional dependence on microvessel diameter as it does on flow velocity. At a distance of 30 mm from the magnet, the percentage of tested cases where at least 50% of the microbubbles were captured is 58%. This decreases with distance to the magnet to 33% at 40 mm and 8% at 50 mm.

#### D. Real-time monitoring of microbubble capture in a flow phantom

Real-time monitoring using B-mode and PICEUS was demonstrated on a single channel tissue-mimicking flow phantom. Single frames captured from the experiment at the start of flow (0 min), at the midway point (3 min), and at the end (6 min) are shown in Fig. 8. In the images, the CMUT is positioned at the top. To ensure an even comparison, all images shown were normalised to the maximum brightness observed during operation of each mode, which for both B-mode and PICEUS occurred in the frame at 3 min with the magnet in place (Fig. 8e and Fig. 8k, respectively). The black levels were then adjusted so that both B-mode and PICEUS images span a dynamic range in intensity of 38 dB.

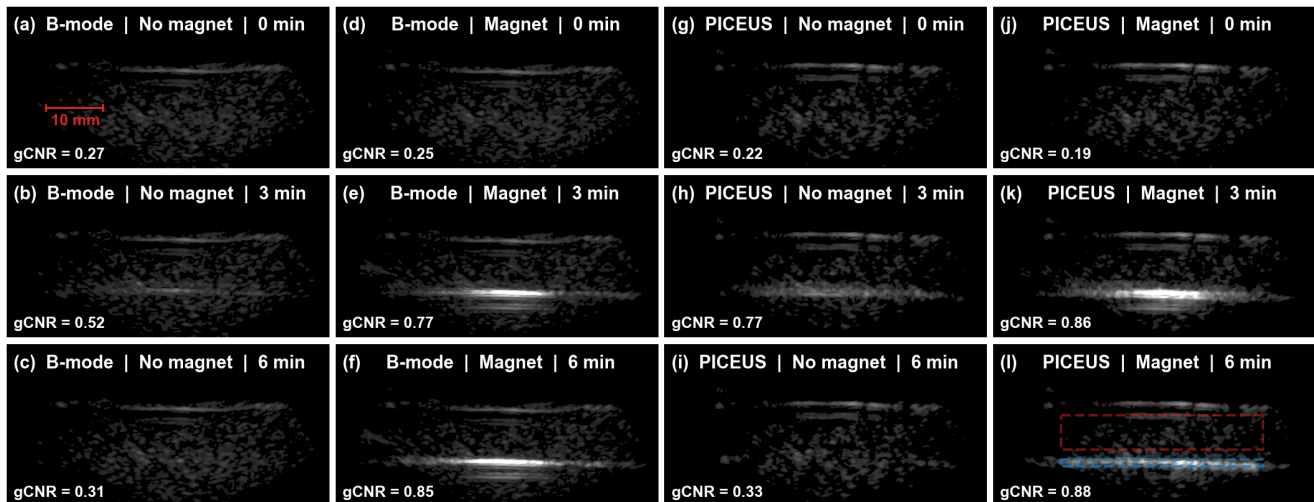


Fig. 8. Real-time monitoring of magnetic capture in a flow phantom. (a)-(f) B-mode images with and without the magnet at 0, 3, and 6 minutes. (g)-(l) PICEUS images with and without the magnet at 0, 3, and 6 minutes. The dynamic range of all images is 38 dB. Generalised CNR was used to quantify the detectability of the flow channel from the background, where the red and blue dashed rectangles indicate the ROIs corresponding to the background speckle and channel, respectively.

Prior to the start of flow, the PBS-filled channel was not distinguishable in either B-mode or PICEUS images due to the similar acoustic impedances of the fluid and the phantom material and because of the significant speckle contrast of the phantom material. After the start of flow, for each trial, it took between 40 to 60 seconds for the microbubble bolus to reach the phantom, confirmed visually by an observed increase in contrast. By 3 min, in both trials with and without the magnet, the channel was clearly distinguishable from the surrounding material due to the flowing microbubbles. However, in cases with the magnet present, a region of significant echogenicity appears in front of the magnet, suggesting that microbubbles were successfully retained along the channel wall during flow. At 6 min, with the flow arrested, these bright regions persisted in the cases with the magnet, while the contrast in the channel returned to their pre-bolus levels in cases without the magnet. These results confirm successful retention of flowing microbubbles by the magnet and that our system can provide real-time visualisation for monitoring purposes. Capture performance in this phantom, with a mean flow velocity of approximately 4 mm/s, was better than that predicted by Monte Carlo simulations, possibly due to the absence of buoyancy along the magnet axis, accumulation over a longer time period, and microbubble-microbubble interactions not accounted for in simulation.

Generalised Contrast-to-Noise ratio (gCNR) [38], which ranges from 0 to 1, was adopted to quantify the detectability of the microbubble-filled channel from the surrounding background speckle. The ROIs used in the calculation for the channel and background are outlined in Fig. 8 by red and blue dashed rectangles, respectively. With the magnet in place, the probability of detection was improved by 0.25 in B-mode and 0.09 in PICEUS during flow, and 0.54 in B-mode and 0.55 in PICEUS after flow was arrested. The improvement supports the assertion that the magnet was successful in retaining mi-

crobubbles in the channel. Furthermore, during flow, PICEUS improved the detectability of the channel in comparison to B-mode by 0.25 without the magnet and 0.09 with the magnet. At the end of flow, the advantage of PICEUS is diminished with an improvement of only 0.03 in gCNR, which is substantiated visually by the lower but more evenly distributed brightness within the channel ROI. It is hypothesised that because the effective pulse repetition frequency of focused waves to the channel was 3 times lower in B-mode due to multi-zone focusing, microbubble destruction occurred more frequently during PICEUS leading to a smaller less-concentrated population at the end of flow.

## VI. DISCUSSION

The effectiveness of magnetic targeting hinges on both the ability to generate high gradient magnetic fields at depth and to load therapeutic agents with sufficient magnetic material. The results of the present study indicate that our low-cost approach using permanent magnets is capable of generating sufficient field gradients to overcome buoyancy forces at distances up to 35 mm. However, the opposing flow velocity in which the pull force is effective drops off rapidly due to the diminishing field gradient, highlighting one of the challenges of magnetic targeting using a hand-held device.

Despite the diminishing pull force at distance, magnetic retention of microbubbles may be possible in the vascular networks of tumours due to their irregular morphology, small microvessel diameters, and low flow rates. From simulated capture studies covering a range of tumour microvessel diameters and physiological flow rates, it is estimated that our platform could be suitable for targeting tumours at depths of 30 - 40 mm. The system may be effective at 50 mm as well but for a more limited range of flow rates below 1 mm/s and microvessel diameters below 10  $\mu$ m. This would correspond with the capillary network in a tumour [39], for example.

Our studies also illuminate a number of potential improvements that could be implemented to increase the effectiveness of magnetic targeting. For enhancements to the magnetic system, a machined magnet processed from a single high-grade sintered neodymium blanks could be used to better match the optimised target designs at the expense of increased cost and manufacturing complexity. Machined magnets could also improve integration with the CMUT, reducing the gap between the magnet and skin level. Unfortunately, it appears that  $\sim 500$  cc magnet volume is around the limit for comfortable hand-held operation. Larger magnet volumes for targeting at depths of 50 mm and beyond would likely necessitate the use of engineered mounting arm solutions.

For enhancements to the magnetic microbubbles, the key areas warranting further optimisation are reduction of the buoyancy force, increase in SPION loading efficiency, and reduction in fluid drag. Some of these may be realisable from improvements to the formulation and through better control of the microbubble diameter, e.g. via microfluidics. Other areas of further investigation include methods to deliberately induce the formation of microbubble trains which we observed to have improved magnetic loading to drag force ratios, and magnetic filtering techniques whereby microbubble populations are exposed to a strong magnetic field and weaker microbubbles removed physically.

## VII. CONCLUSION

In summary, we have reported on the development of a hand-held probe for a magnetic drug delivery system with integrated real-time monitoring. The system's primary features are its low-cost design based on self-assembling, off-the-shelf permanent magnets, its conformation with a hand-held form factor, and its standard connector design compatible with commercial ultrasound imaging platforms. We demonstrated, through terminal velocity measurements, that our system is capable of attracting magnetic microbubbles against buoyancy at distances up to 35 mm, and, through simulation, may be effective at targeting some tumour vascular networks at distances up to 50 mm. Finally, we showcased the system's real-time monitoring capability by performing B-mode and PICEUS imaging of microbubble retention in a tissue-mimicking flow phantom.

## REFERENCES

- [1] P. M. Price, W. E. Mahmoud, A. A. Al-Ghamdi, and L. M. Bronstein, "Magnetic drug delivery: Where the field is going," *Front Chem*, vol. 6, p. 619, Dec. 2018.
- [2] L. C. Barnsley, D. Carugo, J. Owen, and E. Stride, "Halbach arrays consisting of cubic elements optimised for high field gradients in magnetic drug targeting applications," *Phys. Med. Biol.*, vol. 60, pp. 8303–8327, Nov. 2015.
- [3] L. C. Barnsley, M. D. Gray, E. Beguin, D. Carugo, and E. Stride, "A combined Magnetic-Acoustic device for simultaneous, coaligned application of magnetic and ultrasonic fields," *Adv. Mater. Technol.*, vol. 3, p. 1800081, July 2018.
- [4] O. Baun and P. Blümmler, "Permanent magnet system to guide superparamagnetic particles," *J. Magn. Magn. Mater.*, vol. 439, pp. 294–304, Oct. 2017.
- [5] P. Blümmler, R. P. Friedrich, J. Pereira, O. Baun, C. Alexiou, and V. Mailänder, "Contactless Nanoparticle-Based guiding of cells by controllable magnetic fields," *Nanotechnol. Sci. Appl.*, vol. 14, pp. 91–100, Apr. 2021.
- [6] C. Alexiou, D. Diehl, P. Henninger, H. Iro, R. Rockelein, W. Schmidt, and H. Weber, "A high field gradient magnet for magnetic drug targeting," *IEEE Trans. Appl. Supercond.*, vol. 16, pp. 1527–1530, June 2006.
- [7] F. Mishima, S.-I. Takeda, Y. Izumi, and S. Nishijima, "Development of magnetic field control for magnetically targeted drug delivery system using a superconducting magnet," *IEEE Trans. Appl. Supercond.*, vol. 17, pp. 2303–2306, June 2007.
- [8] S.-I. Takeda, F. Mishima, S. Fujimoto, Y. Izumi, and S. Nishijima, "Development of magnetically targeted drug delivery system using superconducting magnet," *J. Magn. Magn. Mater.*, vol. 311, pp. 367–371, Apr. 2007.
- [9] O. Felfoul, A. T. Becker, G. Fagogenis, and P. E. Dupont, "Simultaneous steering and imaging of magnetic particles using MRI toward delivery of therapeutics," *Sci. Rep.*, vol. 6, p. 33567, Sept. 2016.
- [10] M. Muthana, A. J. Kennerley, R. Hughes, E. Fagnano, J. Richardson, M. Paul, C. Murdoch, F. Wright, C. Payne, M. F. Lythgoe, N. Farrow, J. Dobson, J. Conner, J. M. Wild, and C. Lewis, "Directing cell therapy to anatomic target sites in vivo with magnetic resonance targeting," *Nat. Commun.*, vol. 6, p. 8009, Aug. 2015.
- [11] J. Owen, Q. Pankhurst, and E. Stride, "Magnetic targeting and ultrasound mediated drug delivery: benefits, limitations and combination," *Int. J. Hyperthermia*, vol. 28, no. 4, pp. 362–373, 2012.
- [12] I. Lentacker, I. De Cock, R. Deckers, S. C. De Smedt, and C. T. W. Moonen, "Understanding ultrasound induced sonoporation: definitions and underlying mechanisms," *Adv. Drug Deliv. Rev.*, vol. 72, pp. 49–64, June 2014.
- [13] A. P. McHale, J. F. Callan, N. Nomikou, C. Fowley, and B. Callan, "Sonodynamic therapy: Concept, mechanism and application to cancer treatment," *Adv. Exp. Med. Biol.*, vol. 880, pp. 429–450, 2016.
- [14] M. de Saint Victor, C. Crake, C.-C. Coussios, and E. Stride, "Properties, characteristics and applications of microbubbles for sonothrombolysis," *Expert Opin. Drug Deliv.*, vol. 11, pp. 187–209, Feb. 2014.
- [15] D. Chang, M. Lim, J. A. C. M. Goos, R. Qiao, Y. Y. Ng, F. M. Mansfeld, M. Jackson, T. P. Davis, and M. Kavallaris, "Biologically targeted magnetic hyperthermia: Potential and limitations," *Front. Pharmacol.*, vol. 9, p. 831, Aug. 2018.
- [16] J. Wu, H. Leong-Poi, J. Bin, L. Yang, Y. Liao, Y. Liu, J. Cai, J. Xie, and Y. Liu, "Efficacy of contrast-enhanced US and magnetic microbubbles targeted to vascular cell adhesion molecule-1 for molecular imaging of atherosclerosis," *Radiology*, vol. 260, pp. 463–471, Aug. 2011.
- [17] Y. Heun, S. Hildebrand, A. Heidsieck, B. Gleich, M. Anton, J. Pircher, A. Ribeiro, O. Mykhaylyk, D. Eberbeck, D. Wenzel, A. Pfeifer, M. Wornle, F. Krötz, U. Pohl, and H. Mannell, "Targeting of magnetic nanoparticle-coated microbubbles to the vascular wall empowers site-specific lentiviral gene delivery in vivo," *Theranostics*, vol. 7, pp. 295–307, Jan. 2017.
- [18] Y. Sheng, E. Beguin, H. Nesbitt, S. Kamila, J. Owen, L. C. Barnsley, B. Callan, C. O'Kane, N. Nomikou, R. Hamoudi, M. A. Taylor, M. Love, P. Kelly, D. O'Rourke, E. Stride, A. P. McHale, and J. F. Callan, "Magnetically responsive microbubbles as delivery vehicles for targeted sonodynamic and antimetabolite therapy of pancreatic cancer," *J. Control. Release*, vol. 262, pp. 192–200, Sept. 2017.
- [19] M. de Saint Victor, L. C. Barnsley, D. Carugo, J. Owen, C. C. Coussios, and E. Stride, "Sonothrombolysis with magnetically targeted microbubbles," *Ultrasound Med. Biol.*, vol. 45, pp. 1151–1163, May 2019.
- [20] B. Zhang, H. Kim, H. Wu, Y. Gao, and X. Jiang, "Sonothrombolysis with magnetic microbubbles under a rotational magnetic field," *Ultrasonics*, vol. 98, pp. 62–71, Sept. 2019.
- [21] E. Beguin, M. D. Gray, K. A. Logan, H. Nesbitt, Y. Sheng, S. Kamila, L. C. Barnsley, L. Bau, A. P. McHale, J. F. Callan, and E. Stride, "Magnetic microbubble mediated chemo-sonodynamic therapy using a combined magnetic-acoustic device," *J. Control. Release*, vol. 317, pp. 23–33, Jan. 2020.
- [22] L. C. Barnsley, D. Carugo, and E. Stride, "Optimized shapes of magnetic arrays for drug targeting applications," *J. Phys. D Appl. Phys.*, vol. 49, p. 225501, May 2016.
- [23] D. T. Margulies, F. T. Parker, F. E. Spada, R. S. Goldman, J. Li, R. Sinclair, and A. E. Berkowitz, "Anomalous moment and anisotropy behavior in  $\text{Fe}_3\text{O}_4$  films," *Phys. Rev. B Condens. Matter*, vol. 53, pp. 9175–9187, Apr. 1996.
- [24] L. C. Barnsley, D. Carugo, M. Aron, and E. Stride, "Understanding the dynamics of superparamagnetic particles under the influence of high field gradient arrays," *Phys. Med. Biol.*, vol. 62, pp. 2333–2360, Mar. 2017.

- [25] J. J. Kwan and M. A. Borden, "Lipid monolayer collapse and microbubble stability," *Adv. Colloid Interface Sci.*, vol. 183-184, pp. 82–99, Nov. 2012.
- [26] G. Bradski, "The OpenCV Library," *Dr. Dobbs's Journal of Software Tools*, 2000.
- [27] R. K. Jain and T. Stylianopoulos, "Delivering nanomedicine to solid tumors," *Nat. Rev. Clin. Oncol.*, vol. 7, pp. 653–664, Nov. 2010.
- [28] J. C. Forster, W. M. Harriss-Phillips, M. J. Douglass, and E. Bezak, "A review of the development of tumor vasculature and its effects on the tumor microenvironment," *Hypoxia (Auckl)*, vol. 5, pp. 21–32, Apr. 2017.
- [29] B. Endrich, M. Intaglietta, H. S. Reinhold, and J. F. Gross, "Hemodynamic characteristics in microcirculatory blood channels during early tumor growth," *Cancer Res.*, vol. 39, pp. 17–23, Jan. 1979.
- [30] M. Leunig, F. Yuan, M. D. Menger, Y. Boucher, A. E. Goetz, K. Messmer, and R. K. Jain, "Angiogenesis, microvascular architecture, microhemodynamics, and interstitial fluid pressure during early growth of human adenocarcinoma LS174T in SCID mice," *Cancer Res.*, vol. 52, pp. 6553–6560, Dec. 1992.
- [31] W.-C. Lin, C.-C. Wu, T.-C. Huang, W.-C. Lin, B. Y.-C. Chiu, R.-S. Liu, and K.-P. Lin, "Red blood cell velocity measurement in rodent tumor model: An in vivo microscopic study," *J. Med. Biol. Eng.*, vol. 32, pp. 97–102, Apr. 2012.
- [32] P. N. Brown, G. D. Byrne, and A. C. Hindmarsh, "VODE: A Variable-Coefficient ODE solver," *SIAM J. Sci. and Stat. Comput.*, vol. 10, pp. 1038–1051, Sept. 1989.
- [33] I. Ladabaum, X. Jin, H. T. Soh, A. Atalar, and B. T. Khuri-Yakub, "Surface micromachined capacitive ultrasonic transducers," *IEEE Trans. Ultrason. Ferroelectr. Freq. Control*, vol. 45, no. 3, pp. 678–690, 1998.
- [34] S. Satir and F. L. Degertekin, "Phase and amplitude modulation methods for nonlinear ultrasound imaging with CMUTs," *IEEE Trans. Ultrason. Ferroelectr. Freq. Control*, vol. 63, pp. 1086–1092, Aug. 2016.
- [35] C.-C. Shen, Y.-H. Chou, and P.-C. Li, "Pulse inversion techniques in ultrasonic nonlinear imaging," *J. Med. Ultrasound*, vol. 13, pp. 3–17, Jan. 2005.
- [36] C. C. Shen and P. C. Li, "Harmonic leakage and image quality degradation in tissue harmonic imaging," *IEEE Trans. Ultrason. Ferroelectr. Freq. Control*, vol. 48, pp. 728–736, May 2001.
- [37] K. V. Ramnarine, T. Anderson, and P. R. Hoskins, "Construction and geometric stability of physiological flow rate wall-less stenosis phantoms," *Ultrasound Med. Biol.*, vol. 27, pp. 245–250, Feb. 2001.
- [38] A. Rodriguez-Molares, O. M. H. Rindal, J. D'hooge, S.-E. Masoy, A. Austeng, M. A. Lediju Bell, and H. Torp, "The generalized Contrast-to-Noise ratio: A formal definition for lesion detectability," *IEEE Trans. Ultrason. Ferroelectr. Freq. Control*, vol. 67, pp. 745–759, Apr. 2020.
- [39] E. N. Marieb and K. Hoehn, *The cardiovascular system: blood vessels*. Pearson Education, 2013.